Applied Energy 344 (2023) 121272

Contents lists available at ScienceDirect

Applied Energy

journal homepage: www.elsevier.com/locate/apenergy

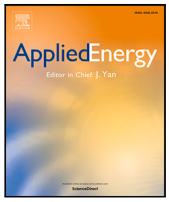

Beyond 15 MW: A cost of energy perspective on the next generation of drivetrain technologies for offshore wind turbines

Garrett E. Barter [a,*], Latha Sethuraman [a], Pietro Bortolotti [a], Jonathan Keller [a], David A. Torrey [b]

[a] National Renewable Energy Laboratory, 15013 W. Denver Parkway, Golden, 80401, CO, United States
[b] GE Research, 1 Research Cir, Niskayuna, NY, 12309, United States

ARTICLE INFO

Keywords:
Permanent magnet synchronous generator
Superconducting generator
Direct drive
Medium speed
Levelized cost of energy
Offshore wind

ABSTRACT

Leading wind turbine manufacturers are racing to build larger and more powerful offshore machines. Drivetrain configurations often use a permanent-magnet synchronous generator (PMSG), in either a direct-drive configuration or coupled to a gearbox. With increasing demand for critical rare-earth magnets, new generator technologies are emerging to ensure a stable and secure supply chain. We evaluate three different topologies of radial flux synchronous generators employing high field magnets with reduced or no rare-earth content: a direct-drive interior PMSG (DD-IPMSG), a geared drivetrain combining a medium speed gearbox with a PMSG (MS-PMSG), and a direct-drive low-temperature superconducting generator (DD-LTSG). We develop a conceptual design module for each of these technologies within a larger framework for full turbine design. This provides the fairest comparison between technologies at nominal power ratings from 15–25 MW, which represent the next generation of offshore wind turbines. The analyses show that if operational expenditures (OpEx) are constant across the technologies, MS-PMSG results in the lowest LCOE with reductions of up to 7% relative to DD-IPMSG. DD-LTSG also yields lower LCOE values by 2%–3% for fixed-bottom turbines and 3%–5% with a floating platform. However, results are sensitive to OpEx assumptions, with a mere 10% increase causing the conclusions to shift.

1. Introduction

In recent years, installations of offshore wind farms with fixed-bottom foundations have grown steadily. Paired with the maturation of floating platform technology, the expected cumulative installed power will reach approximately 270 gigawatts (GW) globally by 2031 [1]. This expansion in installed capacity has been tightly coupled with the steady growth in commercial wind turbine ratings. With recent availability of larger and more powerful turbines nearing 15 megawatts (MW), the levelized cost of energy (LCOE) for offshore wind is projected to be less than $85 (USD) per megawatt-hour (MWh) by around 2024 [1]. As wind turbine ratings increase, individual components must also scale, with different physics and logistical drivers impacting each component in a unique way. For the drivetrain, sustaining this growth pathway and meeting the surging demand for raw materials, especially for critical rare-earth magnetic elements, is forcing several wind farm developers and leading turbine manufacturers to diversify their sourcing [2]. This diversification involves simultaneously investing in efficiency improvements and using advanced technologies that have a more secure supply chain, reduced capital costs, lower operations and maintenance (O&M) costs, and extended lifetimes.

1.1. Recent trends in generators for offshore wind turbines

Thus far, leading manufacturers in the offshore wind energy market have favored either a direct-drive interior permanent-magnet synchronous generator (DD-IPMSG) or a compact PMSG coupled to a medium-speed gearbox (MS-PMSG) [3]. PMSG-oriented designs likely have staying power in the marketplace, as they are low risk and cost-competitive. Furthermore, there are long-term efforts to realize PMSG designs that also eliminate rare-earth permanent magnets [4].

Choosing a suitable generator configuration is a system-level decision because it directly impacts the overall performance of the wind turbine as well as the costs. Most PMSGs used for high power ratings in wind turbines have a radial flux topology with surface-mounted magnets. This surface-mounted permanent-magnet (SPM) configuration helps achieve high-torque densities, acceptable air-gap-flux densities, low-torque ripple enabled by a large range of available pole numbers, and straightforward manufacturing. Slabs of magnets are glued to the rotor surface with an adhesive and supported by additional mechanical strapping for retention. To avoid demagnetization risks, surface mounting often necessitates the use of thicker magnets and enhanced thermal

* Corresponding author.
E-mail address: garrett.barter@nrel.gov (G.E. Barter).

https://doi.org/10.1016/j.apenergy.2023.121272
Received 4 February 2023; Received in revised form 29 April 2023; Accepted 9 May 2023

control mechanisms [5]. Unfortunately, replacing these magnets with ones that have a lower dysprosium content (a rare-earth metal with a particularly challenging supply chain) increases the risk of partial irreversible demagnetization. For instance, some commercially available dysprosium-free neodymium-iron-boron ($Nd_2Fe_{14}B$) magnets have an energy product approaching 55 Mega-Gauss-Oersted (MGOe), albeit with a risk of high magnet losses, partial irreversible demagnetization, and concerns over robustness, which result in heavier generator designs [6]. While the remanence of these reduced dysprosium magnets will be sufficient to provide the needed air-gap flux density, the reduced coercivity can be overcome by embedding the magnets in slotted cavities in the generator rotor, enabling easier alignment and better retention, without the need for special tooling. These interior PMSG generators (IPMSGs) with fractional-slot concentrated windings (FSCWs) are therefore a promising option for large-scale wind power generation [7].

Magnets arranged in a V-shaped configuration augment the permanent-magnet torque (and power output) with reluctance torque via enhanced magnetic flux concentration and higher saliency. FSCWs can further enhance the performance with a high slot-fill-factor, short end-turn, high-efficiency, and low-torque ripple. While IPMSGs may have inherent protection against demagnetization, the use of high pole counts can be limited due to finite space in the rotor frame and large leakage flux. Further, the reluctance torque of IPMSG machines with FSCWs can be lower than that of traditional distributed winding layouts. Preliminary studies comparing a 7 MW SPM to an IPM PMSSG showed that the IPM generator has higher torque per volume and less magnet loss than the SPM generator [8].

In a medium-speed configuration, newer gearbox designs are emerging with a higher step-up ratio of the rotor speed compared to traditional two-stage planetary gearbox designs [9]. This approach allows for significantly smaller PMSGs and capital costs when compared to a direct-drive architecture, but also comes with operational expenses associated with gearbox maintenance, which are especially costly in an offshore setting. On the other hand, a direct-drive approach that seeks to avoid gearbox maintenance costs faces a significant challenge in scaling a PMSG to the next generation of wind turbines with power ratings approaching 20 MW or greater. At those scales, a radial-flux PMSG becomes extremely heavy, with significant magnet mass, meaning it is also quite costly and stresses the rare-earth supply chain by a greater extent [10]. Both the increased O&M costs and mass penalties can be particularly daunting in an offshore setting, challenging both the project economics and vessel requirement logistics for installation and maintenance activities. For floating platforms, generator weight has a cascading impact on cost, as greater tower-top mass means greater mass below the waterline to meet stability requirements. The use of advanced technologies, such as high field magnets enabled by superconductors, promises significant weight reduction even in a direct-drive configuration. Superconducting generators therefore have the appeal of supporting wind turbine upscaling without a significant weight penalty, which also makes them more attractive for floating applications [11].

1.2. Superconducting generators

In recent years, significant progress has been made in the manufacturing of superconductors and the related cryogenic and refrigeration technology, creating new opportunities for realizing ultra-efficient wind turbine generators with a more secure raw-material supply chain. For instance, critical current prices have fallen from $150 per kiloAmpere/meter (kA/m) in 2014 to $83/kA/m in 2019 [12]. At present, the two main types of superconductors available in the market are the low-temperature superconductor (LTS) and high-temperature superconductor (HTS). Both approaches show promise in terms of material characteristics, price, and relevant cryogenic and refrigeration system. In fact, commercially available conductors can handle magnetic fields higher than 10 Tesla (T). Because these technologies promise higher torque density and efficiency with high magnetic loading and electric loading, when compared to traditional PMSGs, they will always be tantalizing for wind turbine manufacturers. Steady improvements in cryogenic and refrigeration technologies and availability of commercialized Niobium Titanium (NbTi) and Niobium Tin (Nb3Sn) wires at lower costs as alternatives to rare-earth Barium Cobalt (ReBCO) or Yttrium Barium cobalt (YBCO) conductors, have prompted renewed interest. These improvements have been largely driven by other industries, such as LTS wires that are mass produced and used in magnetic resonance imaging devices or an HTS accelerator and fusion magnets. As yet, HTS conductors are limitated in terms of mechanical strength, with significant critical current degradation even at a small strain of less than 0.5% [13] that can impose challenges in precision winding. This limitation has delayed the needed level of maturation of large-scale manufacturing for HTS conductors. Further, to the knowledge of the authors, there are no reliable protection mechanisms known to exist against quench (the transition from the superconducting state to the resistive state, during which the magnetic energy is turned into thermal energy) for the large-size, high-magnetic-energy HTS coils.

The use of superconducting generators (SCGs) in wind turbines has so far been limited to conceptual design studies and proof-of-concept prototypes. However, without detailed design or operational experience, the full system impacts on the rest of the turbine are not fully understood. This limited understanding is especially true at the large power ratings, because the turbines themselves are conceptual as well. It is therefore difficult to arrive at a conclusive levelized cost of energy (LCOE) comparison between PMSG- and SCG-based wind turbines. Hence, it is still unclear as to where SCGs might be the most competitive compared to PMSGs. Prior work in the literature is limited and offers a range of comparisons and results that do not fully agree.

In 2018, the INNWIND project directed conceptual studies for an HTS generator based on magnesium diboride (MgB_2) and ReBCO conductors compared to permanent-magnet-based generators for a 20 MW reference wind turbine [14]. The results showed that the LCOE of the HTS generator was not competitive with a traditional MS-PMSG drivetrain, mainly due to the high costs of the superconductors, cryostats, and cooling systems that were in early stages of industrialization. Another LCOE evaluation through the EolSupra20 project [15], showed that a fully superconducting wind turbine generator could be cost competitive to a traditional DD-PMSG for a 20 MW floating wind turbine, if the price of the superconducting wire were to decrease. A similar outcome was found in a scaling study by Jung et al. [12], who concluded that a 40% reduction in conductor costs was necessary for HTS generators to compete with DD-PMSG at 10 MW. In 2019, the EcoSwing consortium successfully designed, built, and field tested a 3.6 MW HTS generator for the land-based wind market [16]. The prototype generator was 40% smaller and 15% cheaper than the baseline, with only about 1 kilogram (kg) of rare-earth material per megawatt, compared to 650–1000 kg/MW for a DD-PMSG or 160 kg/MW for a MS-PMSG [17]. The EcoSwing generator successfully produced 1 MW of electric power utilizing about 10 kilometers (km) of HTS tape made of YBCO.

As a technology that is still in development, with different architectures being actively pursued by different groups, there is still plenty of room for further design maturation of superconducting generators to lower the capital costs of active materials [18]. Preliminary results considering the performance and cost of the superconducting wires and cryogenic and refrigeration system for generators with both HTS and LTS field windings were reported in Wang et al. [19]. The study reported that LTS-based generators were more favorable in terms of initial capital, technology maturity, and engineering feasibility. Other examples of superconducting technology and topology exploration, in addition to LTS vs. HTS options, include the transition from iron-core machines to air-core and partially superconducting to fully superconducting generators [20].

1.3. Article contributions

In this article, we compare wind turbines and plants with an SCG versus DD-IPMSG and MS-PMSG technology. Instead of looking at a single design point, we consider a range of design turbine rating points between 15 and 25 MW. Our goals are similar to that of Hoang et al. [21], who identified DD-PMSG to be more competitive for power ratings below 8 MW and DD-HTSG for power ratings exceeding 8 MW. This work goes further not only by including an MS-PMSG design in the comparison, but also in doing a full wind turbine system redesign around the generator technologies. Meaning, the rotor operating curve, drivetrain sizing, and support structure are customized to the mass and efficiency of each generator option. Furthermore, we consider both fixed-bottom and floating platform projects, as the mass scaling properties may have more of an impact on floating platforms.

For the SCG technology comparison we consider a low-temperature superconducting generator (LTSG) approach for a few reasons. First, based on industry experience around magnetic resonance imaging (MRIs), LTS technology has a higher technology maturity, commercial readiness, and availability. This maturity means that today, they have a lower capital expense and more established supply chain, even if the long-term vision is for HTS to be cheaper based on their lighter cryogenic needs. This maturity also means that older studies comparing LTSG to HTSG or PMSG solutions may be out of date and worth revisiting using present-day costs. This statement is equally true for the IPMSG concepts, using reduced dysprosium magnets and a V-shaped magnet arrangement for magnetic field focusing.

2. A systems engineering design approach

This work presents a techno-economic evaluation of three conceptual generator-drivetrain concepts for offshore wind turbines using the National Renewable Energy Laboratory's (NREL's) systems engineering framework, the Wind-Plant Integrated System Design & Engineering Model (WISDEM®) and Wind Energy with Integrated Servo control (WEIS) [22]. Included in the study is a conventional DD-IPMSG, with reduced-dysprosium magnets, a conventional MS-PMSG with reduced dysprosium magnets, and a rare-earth-free DD-LTSG. The objective is to determine which of these generator technologies is the most cost competitive as wind turbine size increases, and whether the answer changes between fixed-bottom and floating foundations.

We conceptually designed and optimized three generator technologies at five different nameplate powers (15 MW, 17 MW, 20 MW, 22 MW, and 25 MW) for both fixed-bottom and floating offshore foundations. This effort resulted in 30 unique design points in our test matrix. To guide the optimization algorithm, each generator technology was designed around a target efficiency at the rated operating condition.

For all designs, the 15 MW offshore reference wind turbine released by the International Energy Agency Wind Task 37 on Systems Engineering in its monopile fixed-bottom [23] and semisubmersible floating configuration [24] served as the starting point. Several specifications of the 15 MW reference wind turbine were kept constant. These specifications include the specific power and maximum blade tip speeds, which were set at 325 watts per square meter (W/m^2) and 95 meters per second (m/s), and also the airfoils, materials, blade composite topology, and overall configuration (three-bladed upwind turbine). For the floating foundation, the semisubmersible column sizes and offset distances were sized for each design, but the overall architecture remained fixed. Some of the key rotor design parameters are listed in Table 1. Once the rotor and generator designs were complete, the remainder of the drivetrain, then the tower and foundation were completed as well.

The following sections describe the various component design optimizations in greater detail.

Table 1
Key rotor design parameters for the conceptual wind turbines in this study. Maximum blade tip speed and specific power are constant across designs at 95 m/s and 325 W/m^2. Shaft torque is computed at a generator efficiency of 95%.

		Nameplate power (MW)				
Parameter	Units	15	17	20	22	25
Rotor diameter	m	242.2	257.9	279.7	293.36	312.7
Blade length	m	117.2	124.7	135.3	141.78	151.2
Hub diameter	m	7.9	8.4	9.2	9.8	10.4
Rotor overhang	m	12.0	13.0	14.0	15.0	16.0
Rated rotor speed	rpm	7.5	7.0	6.5	6.2	5.8
Rated shaft torque	MNm	20.1	24.3	31.0	35.8	43.3

rpm: revolutions per minute

Table 2
Key generator configuration parameters for the conceptual designs in this study.

		Generator architecture		
Parameter	Units	DD-LTSG	DD-IPMSG	MS-PMSG
Rotor–stator config		Inner rotor	Outer rotor	Inner rotor
Gear ratio		1:1	1:1	1:120
Target efficiency	%	97	95	96
Rated terminal voltage	kV	3.3	3.3	3.3

2.1. Rotor

We generated five rotor designs at the five nameplate power ratings using the parameters in Table 1. The rotor blade design variables were chord, twist, and spar cap thickness at six equally spaced spline control points along the blade span. Some of the first and last stations were locked to guide the optimizer toward realistic solutions. The figure of merit of the optimization was LCOE (with fixed cost assumptions for the non-varying components). The optimization constraints included:

- Ultimate strains along the spar caps below 3500 microstrains
- Blade tip deflections not exceeding minimum tower clearance
- Flapwise blade root moment coefficient below 0.16 to guide the optimizer toward lightly loaded blade designs, especially in the outer most spanwise sections.

2.2. Generator technologies

The design optimization for all the generator topologies followed a new approach implemented in WISDEM's generator design tool, GeneratorSE [25], that has been coupled with the open-source library, Finite Element Method Magnetics (FEMM) [26] through a Python interface [27]. Fig. 1 shows the eXtended Design Structure Matrix (XDSM) diagram for the coupling scheme between GeneratorSE and FEMM. Each optimization consists of a finite-element evaluation of electromagnetic design followed by analytical estimates for structural deformation, power losses, and total costs that follow certain assumptions. Each generator topology is optimized at the rated shaft torque and speed specified in Table 1, at the target rated efficiency in Table 2 with a stator terminal voltage of 3.3 kilovolts (kV). The rated torque, efficiency, and terminal voltage are posed as design constraints in all cases.

All generator designs were optimized for minimum cost, with the generator cost estimation based on the bill of materials. The mass values for each material were tallied in GeneratorSE and then scaled by a manufacturing waste factor and the cost per unit weight. The bill of materials mass entries were also multiplied by an energy consumption rate and the average price of industrial electricity, $78/MWh, according to the Energy Information Administration. The final generator material cost can be therefore written as,

$$C_m = \sum_i^{N_m} m_i \left(f_i c_i + e_i c_e \right) \tag{1}$$

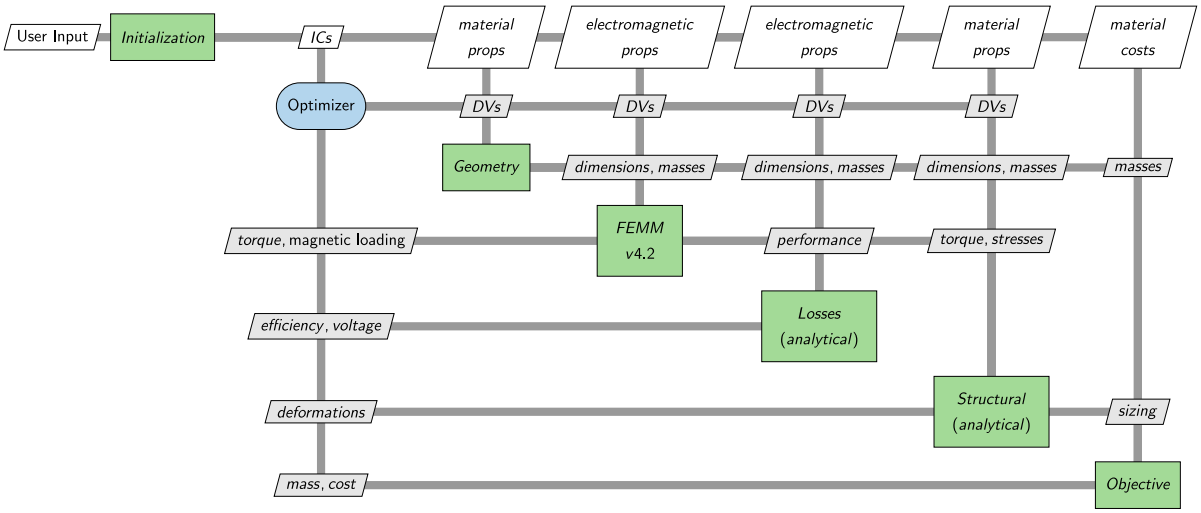

Fig. 1. The eXtended Design Structure Matrix (XDSM) diagram of the FEMM-coupled GeneratorSE design optimization approach.

Table 3
Cost model for the conceptual generator designs.

Material	Unit cost USD/kg	Waste factor –	Energy rate kWh/kg
Copper	7.30	1.26	96.2
Electrical steel	4.44	1.21	26.9
Structural steel	1.56	1.21	15.9
Neodymium (N48SH) magnets	66.72	1.00	79.0
NbTi conductor	45.43	1.00	79.0

Copper prices: http://moneymetals.com/copper-prices
Steel prices: http://agmetalminer.com/metal-prices
Neodymium (NdFeB) prices: http://metal.com/Rare-Earth-Magnets/202103120034
NbTi prices: http://alibaba.com/showroom/superconducting-wire.html
Electricity price: http://eia.gov/electricity/monthly/epm_table_grapher.php?t=epmt_5_6_a

where N_m is the number of materials, m_i is the mass for the ith material, f_i is the waste factor, c_i is the unit cost, e_i is the energy intensity, and c_e is the electricity cost. The material cost model inputs are listed in Table 3, with the waste factor and energy consumption rate calculated by NREL's Materials Flow through Industry (MFI) Tool [28]. The U.S. Bureau of Labor Statistics (BLS) publishes a fractional breakdown between purchased material cost share, labor cost share, and capital cost share for every industry sector in the North American Industry Classification System (NAICS) through their productivity databases [29]. With this information, once the material cost was determined, it was scaled by 1/0.632, as 63.2% is the average fraction of total cost of a finished product from materials and consumables for the energy industry sector. This scaling then indirectly captures the cost contributions from labor and capital amortization or depreciation (e.g., factory tooling). By taking this approach, we therefore assume that the labor and tooling cost rates are equal across all generator technologies.

A key modeling simplification was the omission of any thermal calculation in the analysis or representation of the cooling systems. We acknowledge the additional complexity of the cooling and cryogenic requirements of the DD-LTSG architecture, but we could not accommodate thermal simulation at the appropriate level of fidelity to both resolve the differences between the technologies yet also be amenable to conceptual design optimization. For cooling mass and cost estimation, we simply relied on the regression-based approximations in WISDEM's Cost and Scaling Model for every technology,

$$m_{cool} = 0.025 P \pi D_{gen} \quad (2)$$

$$c_{cool} = 124 m_{cool} \quad (3)$$

where the generator rating, P, is given in kilowatts and is scaled by the approximate outer circumference of the generator in meters. The mass is provided in kilograms and the cost in U.S. dollars, such that the coefficients are 0.025 kg/kW/m and 124 USD/kg, respectively.

Another modeling simplification was the focus on steady-state performance, neglecting transient dynamics and nuances associated with control strategies tailored to each generator technology. We constructed an rpm-efficiency curve assuming a variable-speed generator torque controller to control the generator power and a collective blade pitch controller to regulate rotor speed. A tip speed ratio tracking approach governed Region II operation below rated wind speed and a constant torque approach governed Region III above rated wind speed. An 80% peak thrust shaving was assumed to be in place near rated wind speeds (Region II.5). Beyond this level of detail, it will be necessary to tailor the control strategies to each generator technology. All of the generators are assumed to be excited through voltage source converters that regulate the generator phase currents, consistent with today's standard practice for offshore wind turbines. The DD-IPMSG would be excited to maximize torque per Ampere by making use of both magnet (quadrature current) and reluctance torque (direct and quadrature current). The MS-PMSG and DD-LTS generators do not have magnetic saliency, so torque production is based only on quadrature current.[1] The optimization of each generator adjusts the excitation current to provide required torque and efficiency. However, given our steady-state modeling approach and focus on LCOE-level comparisons between the various architectures, we did not conduct any time-domain performance simulations where these more transient control strategies would be relevant.

In addition to the common objective function of generator cost, all the conceptual designs used a similar optimization strategy. A gradient-free workflow was found to perform much better than using gradient-based optimization algorithms. The limitations of a gradient-based approach are rooted in the grid convergence of the FEMM software. FEMM provides an excellent mesh generator that is tuned to provide rapid engineering accuracy in its results. This "smart mesh" feature, however, does not ensure a grid converged result. Therefore, small perturbations in the geometry can lead to perturbations in mesh quality and solution accuracy that yield physically inaccurate gradients for finite difference calculations. This obstacle could be overcome

[1] The magnet or superconducting field is always on the direct axis. Quadrature current creates torque acting on the field; direct current can be used to weaken or enhance the field, or to generate reluctance torque for generators with magnetic saliency.

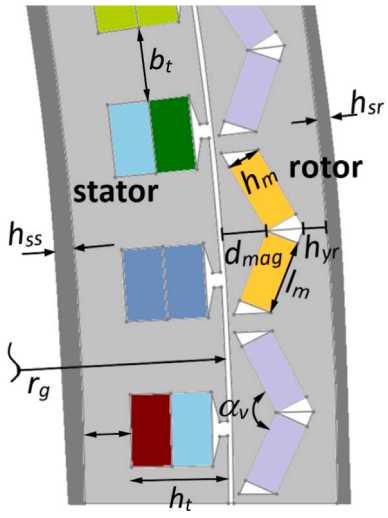

Fig. 2. IPM design parameters.

by using larger finite difference step sizes or higher-order difference schemes, but we found it difficult to arrive at a robust set of algorithm tuning parameters that served each design case. Instead, we opted for a gradient-free workflow with a combination of global search followed by a local neighborhood search. The global search was performed with a differential evolution algorithm available through the OpenMDAO library [30], which also served as the "glue-code" that connected all of the various components in Fig. 1 together. The local neighborhood search was conducted with an implementation of the COBYLA algorithm [31,32] in the NLOpt library [33]. As with any optimization routine, especially when using gradient-free approaches, some degree of restart and iteration was required to ensure a consistent family of designs across the power ratings.

The following subsections describe each generator model. A more complete technical description of the generator models can be found in Sethuraman et al. [34] and the underlying code is open source and publicly available [25].

2.2.1. DD-IPMSG

Among the various IPM topologies, the V-shape radially magnetized designs demonstrate higher power densities and efficiency, lower manufacturing costs, and a wider constant power operating range [35]. Shown in Fig. 2, the configuration offers more opportunities to minimize the required volume of magnets with reduced-dysprosium content while also providing sufficient protection against demagnetization without compromising performance. With an outer rotor architecture, the V-shape IPM topology is easy to assemble, keep cool, and provide robust structural support. These characteristics makes them well-suited to commercial offshore wind energy applications with high-megawatt power ratings. For these reasons, we selected an outer rotor V-shaped IPMSG generator with fractional slot concentrated windings as the most competitive, direct-drive conventional architecture.

Fig. 2 depicts the main design variables used in the DD-IPMSG model, which are based on the outer-rotor configuration for the 15 MW reference generator [23], updated for the V-shape IPM layout. Table 4 lists the design bounds for the variables that are changed during the optimization as the magnet slots assumed different angles. Note that α_v and l_m in Fig. 2 were derived quantities that were determined from the other parameters. We modeled five poles and six slots with anti-periodic boundary conditions. This was the smallest pole-slot combination possible for machine analysis using the chosen boundary conditions, and consistent with the stator winding configuration used in the original 15 MW reference generator. Each rotor pole contains

Table 4
Design variables and bounds for the DD-IPMSG.

Symbol	Description	Units	Bounds	
			Lower	Upper
r_a	Stator radius	m	3	4.75
h_t	Tooth height	mm	40	350
l_s	Axial length	m	0.75	2.5
d_{mag}	Vertex to rotor inner radius	mm	50	250
h_m	Magnet thickness	mm	5	60
h_{yr}	Rotor yoke thickness	mm	20	300
h_{ys}	Stator yoke thickness	mm	20	300
pp	Pole pairs	–	50	200
N_c	Turns per coil	–	2	10
b_t	Tooth width	mm	20	100
J_s	Winding current density	A/mm^2	3	6
h_{ss}	Stator support rim thickness	mm	40	200
h_{sr}	Rotor support rim thickness	mm	40	200
t_r	Rotor disc thickness	mm	50	300
t_s	Stator disc thickness	mm	50	300

a single layer of magnets arranged in a V shape. The ratio of magnet arc-to-pole pitch was assumed to be 0.9. The magnet slots (or bridges) were simplified to a parallelogram with magnets filling the largest rectangular area possible within the available area. No effort was made to optimize the shape of the magnet bridge. The choice of pole pairs influenced the magnet pole arc, magnet V angle (α_v), magnet thickness, and rotor yoke dimension.

The rotor magnets comprise N48SH-grade sintered, reduced dysprosium (smaller than 4% by weight) NdFeB magnets with a remnant flux density of 1.4 T. With the maximum operation temperature limited to 100° C, the knee point for this magnet is slightly below 0.2 T [36].

The stator design uses a three-phase, fractional slot layout and double-layer concentrated coils (with 2/5 slots per pole per phase) with stator tooth height, slot depth, and stack length as the relevant design variables. The stator current density input was capped at 6 A/mm^2 to limit the thermal load on the machine, but no direct thermal simulation was included in the design loop. The phase resistance of the stator winding was calculated assuming a 65% fill factor for copper and the no-load voltage induced by the air-gap flux density in the stator winding were computed using the fundamental space harmonic of the air-gap flux density [37]. The air gap was set at 7 mm.

For the structural design, we used disc-type support structures consistent with the 15 MW reference generator [23]. The air gap was allowed to deflect by up to 20%, with the support structure, shaft, and turret contributing to the deformation. The masses for magnets, stator core and rotor core were derived from cross-sectional areas estimated using the FEMM geometry.

The stator and rotor yokes were assumed to be of M-36 grade steel with a saturation flux density of 2.15 T. It must be noted that the saturation effects in IPMSG can be significant and hence, the peak magnetic loading on the rotor and stator yokes were expressed as design constraints with an upper limit of 2.53 T. In some cases, this constraint was found to be violated near the tooth tips and the region between the magnet bridges of adjacent pole pairs. Each design was evaluated for the minimum magnetic flux density during normal operation and during a three-phase symmetric short circuit and checked against the magnet's knee point.

The iron core losses were approximated with the Steinmetz formula with specific hysteresis losses and the specific eddy current losses assumed at 4 W/kg and 1 W/kg, respectively, in the core. To calculate the total iron losses, the specific iron losses were multiplied by the weight of the iron parts and added together. No effort was made to investigate the influence of magnetomotive force (MMF) space harmonics and eddy current losses in magnets, so the numbers were approximated with assumptions on specific magnet losses.

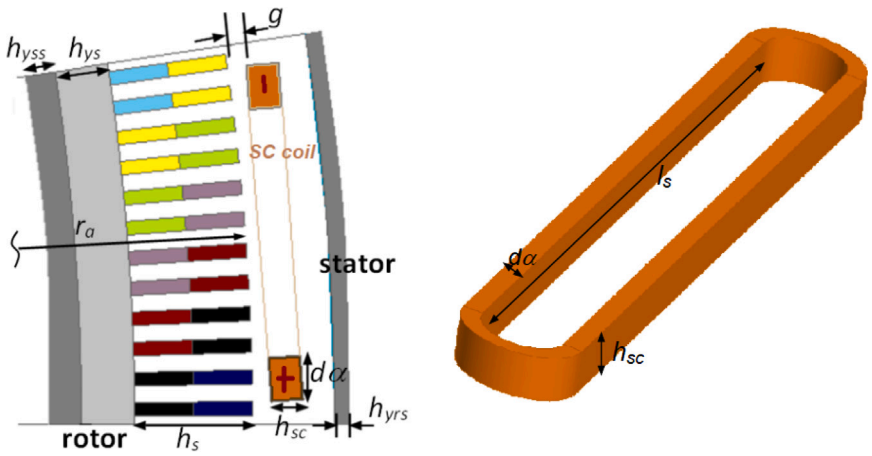

Fig. 3. LTS generator design parameters.

2.2.2. DD-LTSG

We selected an air-core, inner-rotor, radial-flux topology for the DD-LTSG architecture. This topology comprises an inner rotating armature assembly that holds conventional copper windings and an outer stationary field coil assembly of racetrack coils of NbTi conductors working at 4.2 Kelvin (K). The support frame of the armature is connected to the main shaft and power generated is fed via a full-rated converter through slip rings and brushes. The armature windings use a six-phase connection with two sets of three-phase windings displaced by 30°. Non-magnetic material (fiber-reinforced plastic) is assumed for the teeth of armature windings. A magnetic yoke made of silicon steel behind the armature winding serves as a passive shield and improves the coupling between the field and armature. The support frame of the stationary field coil assembly is attached to the bedplate. The LTS field windings used in the generator are racetrack coils wound with NbTi-Cu composite wires with conductor dimensions and critical characteristics provided by Bruker [38]. In modeling the superconducting wires in FEMM, we assumed the superconductor inside a copper matrix with the superconductor occupying a certain volume fraction of the wire (Cu:SC ratio of 4.6). The surrounding medium was assumed to have a relative permeability of 1 and the superconductor has a relative permeability of zero. Then, the apparent bulk permeability was determined using the Ollendorff formula [39] simplified to μ_r=(1−fill)/(1+fill); where fill is the volume fraction of the bulk winding that is occupied by the superconductor.

The armature is forced air cooled to contain the working temperature below 160° Celsius (C). The field coil assembly is cooled by liquid helium such that the helium is in contact with each field coil, around the periphery of the field assembly. As a reminder, no thermal analysis was conducted as part of the conceptual design optimization.

A two-dimensional (2D) FEMM model of a single pole with an odd periodicity boundary condition served as the LTS design model. The key parameters of the LTS model and the racetrack coil are shown in Fig. 3 and Table 5 lists the design variable bounds. The armature winding has a double layer distributed winding layout with two slots per pole per phase to create maximum magnetic symmetry. There are 12 slots per pole and a coil span of 10 slots to achieve a good balance of air-gap harmonics and winding factor. In determining the optimal field coil dimensions, we paid attention to evaluating the feasibility of a given winding geometry, for a given combination of coil width and height including no overlap of the coils. To ensure designs kept to an appropriate stack length, the maximum value of armature flux density was constrained to 2.3 T and measured at the bottom of the non-magnetic teeth. We selected the working point of the superconducting magnets to be within an operating margin that varied between 80%–95% of critical currents. The number of field coil turns is a design variable, and the current is iteratively set by initializing the operating current and computing the maximum flux density within the coil faces by assuming uniform current distribution at zero frequency. We identified the maximum attainable flux density and operating current (I_{sc-op}) via the approach illustrated in Fig. 4. We constructed a linear approximation of the load line by initializing the field current to 650 A. We then offset the critical current characteristics of the wire by an operational safety margin and found the intersection with the load line.

Table 5
Main design variables and bounds for the DD-LTSG.

Symbol	Description	Units	Bounds	
			Lower	Upper
r_a	Stator radius	m	3	4.75
h_s	Winding height	mm	50	400
l_s	Axial length	m	0.75	1.75
h_{sc}	Field coil height	mm	30	250
N_{sc}	Field coil turns	–	1500	3500
h_{yr}	Rotor yoke thickness	mm	150	300
pp	Pole pairs	–	15	40
N_c	Stator turns per coil	–	1	7
$d\alpha$	Wire width	deg	0.2	0.6
h_{ss}	Stator support rim thickness	mm	25	600
h_{sr}	Rotor support rim thickness	mm	25	500
t_r	Rotor disc thickness	mm	25	500
t_s	Stator disc thickness	mm	25	500

We computed the generator phase voltage from the fundamental component of air-gap flux density [37] and scaled it by a factor of 10% to account for contributions from end windings. This correction was determined by comparing the 2D FEMM simulations to more detailed three-dimensional (3D) modeling. The armature winding resistances were computed using a fill factor of 65% of the slots realized by non-magnetic material. With the assumption to ignore thermal modeling, the sizing of the cooling system (i.e., cryogenics, torque tube, and vacuum vessel) was borrowed from a previous study by Richard [40]. The effective air-gap length was held constant at 60 mm to provide a sufficient allowance for these elements that were absent from the FEMM model.

For the structural design, we assumed a 20% deflection limit of the effective air-gap length, similar to the IPM constraints and 15 MW reference generator [23], albeit with swapped rotor and armature arrangements. Generator efficiency was computed considering only winding losses and iron losses in the armature yoke. Winding losses include the resistive losses and brush contact losses. AC losses in the superconducting coils and losses from cryostat walls were neglected due to the large effective air gap and the rapid decay in harmonics [18]. Mechanical losses from bearing friction, windage, and ventilation were

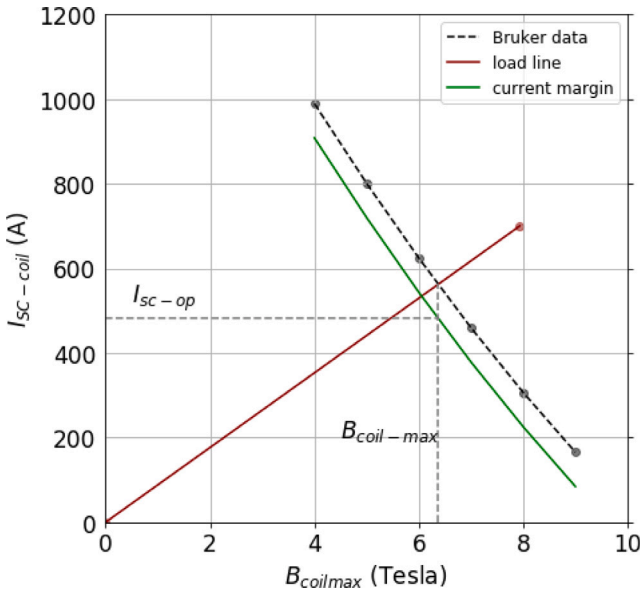

Fig. 4. Operating currents of the superconducting coil for a given dimension with a 10% margin.

approximated to be less than 1% of rated power. Conductor mass and loss estimation for the field and armature coils were calculated using the approach of Liu [18].

2.2.3. MS-PMSG

We selected a radial-flux, surface-mounted PMSG with an inner-rotor topology for the medium-speed configuration, based on the spoked-arm construction presented in Sethuraman and Dykes [37]. Fig. 5 shows a simplified cross-section geometry with the key active and structural design variables listed in Table 6. The 2D FEMM model contained one pole with three slots modeled with a double-layer integer slot winding layout (one slot per pole per phase). Sizing the slots followed the same approach as that of the DD-IPMSG. In sizing the magnet, the magnet thickness was selected for adequate coercive force that is higher than the demagnetizing magneto-motive force during a short circuit. Stator winding current density was limited to be below 6 A/mm^2 and specific current loading to below 65 kA/m to ensure that the temperature rise within the stator and rotor is within permissible values for an air-cooled system. A thermal simulation was not included in the design loop. The structural design consisted of analytical models with constraints for radial, axial, and torsional deformations caused by normal stress, shear stress, and gravity loads.

2.3. Other drivetrain components

The five-turbine rotor designs were integrated with the three generator technologies for a total of 15 drivetrain combinations. Each instance was optimized for other drivetrain parameters, assuming a four-point suspension system (two main bearings). We patterned the direct-drive layout using the 15 MW template, and for the MS-PMSG configuration, we assumed a three-stage gearbox, inspired by Vestas designs [5,9], with a gear ratio of 1:120 at all power ratings and a gearbox torque density of 200 Nm/kg. The optimization sized the main shaft, bearings and bedplate using WISDEM's DrivetrainSE with the SNOPT algorithm [41] to minimize the overall nacelle mass. The design variables for the direct-drive designs were:

- Shaft lengths from the hub to the upwind bearing and from the upwind to downwind bearing
- Diameter and wall thickness of the low-speed shaft
- Diameter and wall thickness of the nose
- Wall thickness of the nacelle bedplate.

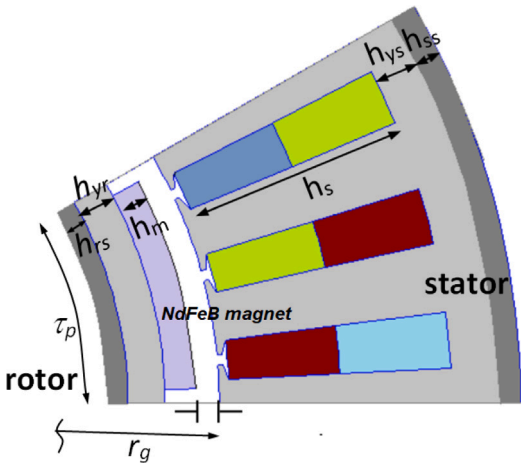

Fig. 5. MS-PMSG design parameters.

The design variables for the medium speed geared designs were:

- Shaft lengths from hub to upwind bearing and from upwind bearing to downwind bearing
- Diameter and wall thickness of the low-speed shaft
- Length, diameter, and wall thickness of the high-speed shaft
- Flange thickness, flange width, and web thickness of bedplate (for an I-beam type support).

Design constraints ensured that von Mises stress criteria were met on low- and high-speed shafts as well as the bedplate. Constraints were also applied on the shaft deflections (linear and angular) at the two main bearing supports. Final constraints were enforced on the layout geometry to ensure that the target rotor overhang was achieved, and on the low-speed-shaft inner diameter to ensure maintenance access.

The optimized drivetrain designs impacted the overall LCOE results in 3 ways: (1) the mass contribution to the tower-top inertial loads that factored into the substructure design, (2) the cost contribution (as estimated by WISDEM) to the turbine capital cost in the LCOE roll up, and (3) the efficiency of the gearbox in the medium-speed configurations contributed to the overall electro-mechanical efficiency.

2.4. Tower and offshore structure

The final step of the wind turbine design process consists of simultaneously optimizing the tower with the support structure: the monopile for fixed-bottom designs and the semisubmersible for floating designs. The monopile and tower were optimized with similar design variables and constraints within WISDEM. For the semisubmersible, we used the frequency-domain model Response Amplitudes of Floating Turbines (RAFT) [42], within the WEIS framework, to execute the design optimization. There were 30 design optimization studies consisting of the 15 rotor nacelle assemblies from the drivetrain optimization step with the two offshore support structure variants. In both cases, the figure of merit was the combined structural mass of the tower and support structure. The tower and monopile were parameterized along their height at 10 points, each in terms of outer diameter and steel wall thickness. Tower and monopile constraints limited the ultimate stress, global and shell buckling (according to DNV guidelines [43]), monotonicity of the profiles, and frequency constraints. The towers for the floating designs had minimum first fore-aft and side-side natural frequencies set to be 20% above the 3P harmonic of the rotor (i.e., the frequency corresponding to three times the turbine rotor rated speed)

Table 6
Design variables and bounds for the MS-PMSG.

Symbol	Description	Units	Bounds	
			Lower	Upper
Electric machine design variables				
r_g	Air-gap radius	m	0.5	2.0
l_s	Axial length	m	0.5	2.5
h_s	Slot height	mm	25	100
g	Air-gap length	mm	6	9
h_m	Magnet height	mm	5	75
pp	Pole pairs	–	4	10
$ratio$	Ratio of pole width to pole pitch	–	0.7	0.85
N_c	Stator turns per coil	–	2	12
I_s	Stator current	A	500	6000
h_{yr}/h_{ys}	Rotor/stator yoke thickness	mm	10	100
Structural design variables				
h_{sr}/h_{ss}	Rotor/stator support rim thickness	mm	45	250
n_r/n_s	Number of rotor/stator spokes	–	5	15
b_r/b_s	Rotor/stator circumferential arm dimension	m	0.1	1.5
d_r/d_s	Rotor/stator arm depth	m	0.1	1.5
t_{wr}/t_{ws}	Rotor/stator arm thickness	mm	1	200

Table 7
Select design optimization results for the DD-IPMSG.

Symbol	Description	Units	Nameplate power (MW)				
			15	17	20	22	25
r_a	Stator radius	m	4.5	4.5	4.75	4.75	4.75
l_s	Axial length	m	2.5	2.5	2.5	2.5	2.5
h_t	Tooth height	mm	107	120	137	149	214
b_t	Tooth width	mm	34.5	32.6	32.5	28.7	33.5
d_{mag}	Vertex to rotor inner radius	mm	50	50	50	50	50
h_m	Magnet thickness	mm	16.3	22.0	30.8	48.3	47.3
h_{yr}	Rotor-yoke thickness	mm	30	97	94	74	81
h_{ys}	Stator-yoke thickness	mm	61.2	48.0	53.8	62.5	115.2
pp	Pole pairs	–	60	65	60	55	55
N_c	Turns per coil	–	4	4	4	4	4
J_s	Winding current density	A/mm^2	6	6	6	6	6
T_{ratio}	Torque ratio	–	1.05	1.01	1.05	1.06	1.05
Ep_{ratio}	Terminal voltage ratio	–	0.81	0.91	0.89	0.82	0.80
η	Efficiency	–	94.7	94.6	94.7	94.9	93.8
M_{gen}	Total mass	t	314.0	382.9	445.9	460.6	507.5
C_{gen}	Total cost	k$	6298.5	7516.0	9334.5	10708.2	11819.7

to avoid a dangerous excitation to the system, a *stiff-stiff* design. Fixed-bottom designs were optimized to lie between 1P and 3P, a *soft-stiff* design. The floater was parameterized in terms of locations of keel and freeboard of main and offset columns. The diameters of the columns were also optimized. The optimizer constrained the maximum platform pitch angle to 5.5°, the metacentric height to 15 m, and ensured adequate water ballast capacity.

All optimizations were driven by the SNOPT solver [41], which was found to be effective in identifying viable solutions in the context of a fairly flat solution space. The optimizer was set to run with a tight tolerance of 1e−6 and maximum number of major iterations of 30 to force the exploration of the design space. Gradients were obtained through central finite differencing.

2.5. LCOE model and optimization

We compare our 30 designs using the terms of the LCOE equation,

$$LCOE = \frac{FCR(CapEx) + OpEx}{AEP} = \frac{FCR(TCC + BOS) + OpEx}{AEP} \quad (4)$$

where the definitions and calculations include the following:

- FCR is the fixed charge rate, an encapsulation of the financing and depreciation adjustments to capital expenses. We use the value of 5.8% from Stehly and Duffy [44] (where greater discussion of FCR can also be found).
- $CapEx$ are capital expenditures required to commission the project.
- TCC is the turbine capital cost, with component contributions of:
  - Blade costs calculated using WISDEM's detailed blade cost model [45].
  - Generator costs calculated as described in Section 2.2.
  - Tower, monopile and semisubmersible costs using the detailed steel manufacturing costs of Farkas and Jármai [46], with additions for waste fraction rates and consumables.
  - All other wind turbine component costs, including drivetrain costs, were calculated using the USD/kg scaling factors in WISDEM's Cost and Scaling Model.
- BOS are the capital expenditures associated with the balance-of-system (or station) activities. We compute a unique value for each of the 30 designs using the Offshore Renewables Balance of System and Installation Tool (ORBIT) [47] connected to WISDEM. This approach takes into account the mass and sizing differences across the various designs as it impacts the number of vessel trips and lifting operations. We assumed a 600 MW offshore wind farm, with varying turbine numbers according to the chosen turbine rating.
- $OpEx$ are the operations and maintenance (O&M) expenditures. We take the recommended values from Stehly and Duffy [44] of $110/kW/yr and $118/kW/yr for fixed-bottom and floating technologies, respectively.

Table 8
Select design optimization results for the DD-LTSG.

			Nameplate power (MW)				
Symbol	Description	Units	15	17	20	22	25
r_a	Stator radius	m	4.5	4.5	4.75	4.75	4.75
h_s	Winding height	mm	148	166	180	220	263
l_s	Axial length	m	1.0	1.0	1.0	1.0	1.0
h_{sc}	Field coil height	mm	40	30	35	45	73
N_{sc}	Field coil turns	–	1504	1506	1606	1806	2102
I_{sc-op}	Field current	A	451.67	527.86	516.47	500.21	514.73
h_{yr}	Rotor yoke thickness	mm	150	150	150	150	150
pp	Pole pairs	–	38	37	39	39	39
N_c	Stator turns per coil	–	1	1	1	1	1
$d\alpha$	Field coil width	deg	0.749	1.316	1.258	1.258	1.310
T_{ratio}	Torque ratio	–	1.02	1.08	0.98	1.02	1.02
Ep_{ratio}	Terminal voltage ratio	–	0.98	0.80	0.84	0.86	0.82
η	Efficiency	–	98.4	98.4	98.5	98.4	98.4
M_{gen}	Total mass	t	192.1	192.9	207.8	217.3	228.6
C_{gen}	Total cost	k$	4944.4	5270.5	6078.9	6631.5	7369.8

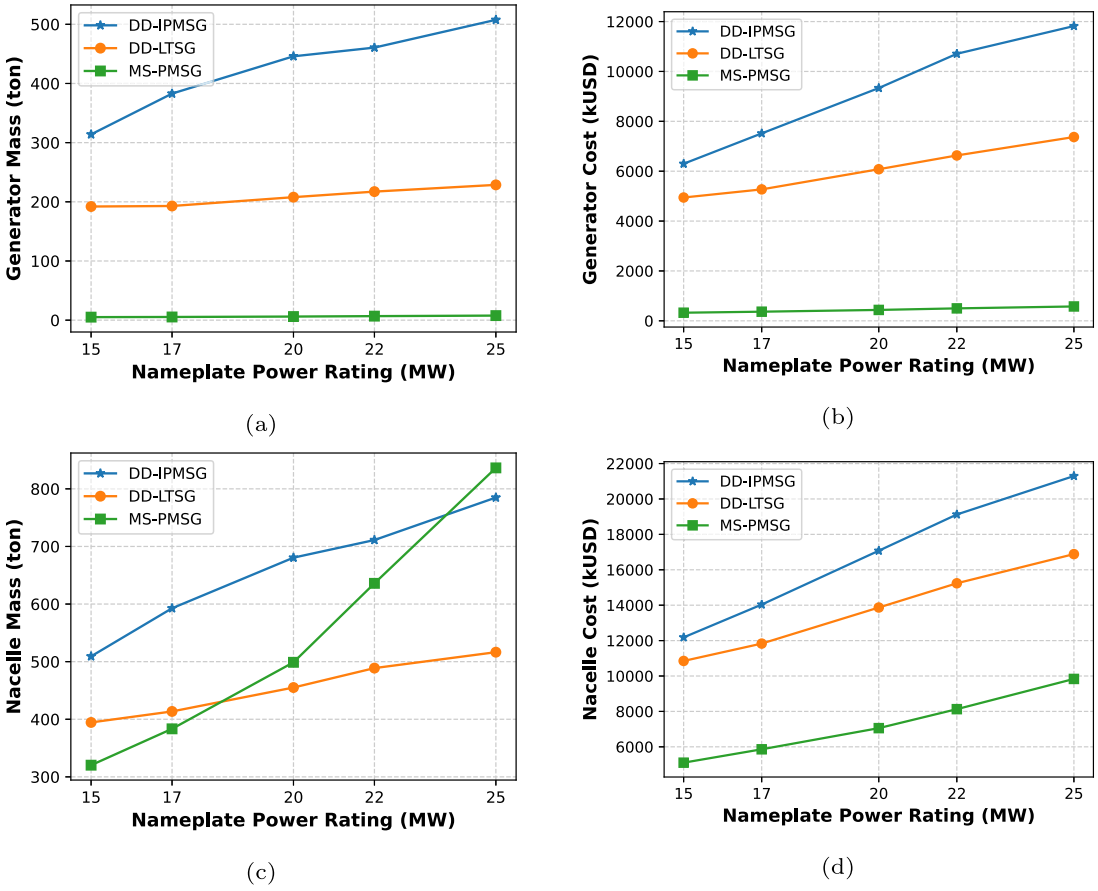

Fig. 6. Generator mass and cost and nacelle mass and cost across drivetrain technologies and nameplate power ratings.

- AEP is the annual energy production, which is the per-turbine AEP computed by WISDEM accounting for rotor and generator performance, multiplied by the number of turbines, and decremented by 15% wake and availability losses.

A significant assumption is that O&M costs are constant across all power ratings and generator technologies. We made this assumption due to the lack of operational data for all technologies at this turbine scale, although in all likelihood it will not be true. There is a possibility that the MS-PMSG architecture will have higher O&M costs due to the addition of the gearbox and there is a possibility that the new DD-LTSG technology could have better or worse reliability compared to a DD-IPMSG. We therefore include a simple sensitivity exploration in the results to show the impact of this assumption, which is relative to the other LCOE terms.

3. Results

This section reports the key results obtained by running the matrix of 30 wind turbine designs in WISDEM and WEIS.

Table 9
Select design optimization results for the MS-PMSG.

Symbol	Description	Units	Nameplate power (MW)				
			15	17	20	22	25
r_g	Air-gap radius	m	0.5	0.5	0.5	0.5	0.5
l_s	Axial length	m	0.59	0.60	0.66	0.69	0.80
h_s	Slot height	mm	25	25	26	26	25
g	Air-gap length	mm	9	9	9	9	9
h_m	Magnet height	mm	12	14	18	28	34
pp	Pole pairs	–	10	10	10	10	10
$ratio$	Ratio of pole width to pole pitch	–	0.83	0.83	0.85	0.85	0.85
N_c	Stator turns per coil	–	2	2	2	2	2
I_s	Stator current	A	6000	6000	6000	6000	6000
h_{yr}	Rotor-yoke thickness	mm	96	81	44	38	45
h_{ys}	Stator-yoke thickness	mm	26	28	35	41	40
T_{ratio}	Torque ratio	–	1.02	0.99	1.00	0.99	0.95
Ep_{ratio}	Terminal voltage ratio	–	1.09	1.07	1.10	1.10	1.20
η	Efficiency	–	0.968	0.972	0.975	0.977	0.977
M_{gen}	Total mass	t	5.116	5.382	6.094	6.810	7.715
C_{gen}	Total cost	k$	325.2	366.1	436.8	499.1	575.7

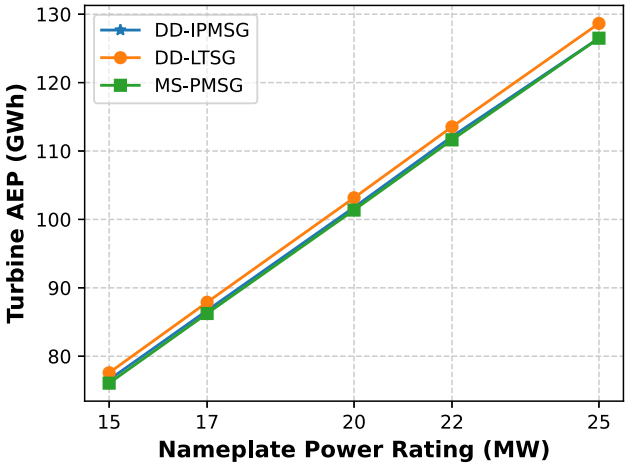

Fig. 7. Wind turbine AEP for the various drivetrain-generator technologies.

3.1. Optimized generator designs

The optimized generator designs are found in Tables 7–9, which list the electromagnetic design variables (structural design details are not shown), the three common constraints across all designs and the summary mass and cost results. The DD-IPMSG-specific results are shown in Table 7. The torque constraint, expressed as a ratio between actual/required, is achieved by all designs as well as the phase voltage constraint, which we allowed to be within 20% of the target value. The reported efficiencies are all slightly below their target value of 95%, with the 25 MW design struggling more than others to meet this requirement. The overall mass of the generator designs scales from 314 tons (t) to as high as 500 t. The efficiency numbers reported here are expected to be sensitive to modeling assumptions around losses. For instance, because no effort was made to optimize the winding distribution and slot opening, the efficiency numbers could be 0.5%–1% lower than what is possible. Further design iteration can improve the efficiencies by optimizing the slot design to minimize eddy current losses from lower order space harmonics of magnetomotive forces.

For the design variables, some are at their bound limits and others are roughly constant. So, the different generators are only distinguished from one another by their stator tooth height, magnet thickness and yoke thickness. The pole counts were rounded off to the nearest integer divisible by five to achieve the required electromagnetic periodicity. Thicker yokes were also found to result in more flux leakage. Because thicker or wider magnets can result in higher air-gap flux density, it can result in reducing the overall weight but at a cost of requiring more magnet material. Overall, we observed some minor variability in the number of pole pairs, but not along a consistent trend.

The DD-LTSG-specific results are shown in Table 8. All three of the constraints are easily satisfied at each design point, including the efficiency at 25 MW, where the DD-IPMSG design struggled. It should also be noted that while the LTSG designs have similar diameters to the DD-IPMSG designs, the axial length is significantly shorter. The overall mass of the generator designs stayed in the close vicinity of 200 t at all power ratings. The reported efficiencies will be reduced by the cryogenic cooling power (typically about 0.3%) and any stray losses in the armature frame. Here too, many of the design variables are at their bounds or otherwise constant across all designs. Differences between the designs can be observed in the field coil height, the number of field coil turns and winding height.

The MS-PMSG-specific results are shown in Table 9. Here too, all three of the constraints are easily satisfied at each design point. Compared to the DD-IPMSG, this finding shows the benefit of the torque-speed trade-off by using a gearbox. The design variables that vary the most significantly by rating are the axial length, magnet height, and yoke thickness.

3.2. Nacelle mass and CapEx

Fig. 6 shows the values of generator mass and cost and nacelle mass and cost across the drivetrain technologies and nameplate power ratings. In terms of generator mass, DD-LTSG reduces mass by 50% compared to DD-IPMSG, with the mass lines diverging at higher power ratings. DD-IPMSG generators tend to get prohibitively heavy and expensive for power ratings larger than 20 MW. The MS-PMSG generator mass and cost appear to be the lightest and cheapest by far, but that is because a significant amount of the total drivetrain complexity has been shifted to the gearbox. Therefore, a more equal comparison is the mass and cost of the nacelle (Figs. 6c–d). In this setting, the DD-LTSG is the lightest, with the MS-PMSG mass growth rate exceeding that of the DD-IPMSG by the 20 MW mark. Nevertheless, the cost of the gearbox is still less per kilogram than a generator, so the MS-PMSG nacelle is still the cheapest overall, followed by the DD-LTSG and then the DD-IPMSG. As a soft validation point for total nacelle mass, a 14 MW commercial wind turbine with a DD-IPMSG configuration reported a total nacelle mass of approximately 500 t, which is consistent with the 15 MW value we report here [48].

3.3. Annual energy production

We did not pursue a modeling approach in this study with sufficient fidelity to resolve the power production differences between fixed-bottom and floating foundations. Therefore, the AEP is the same for

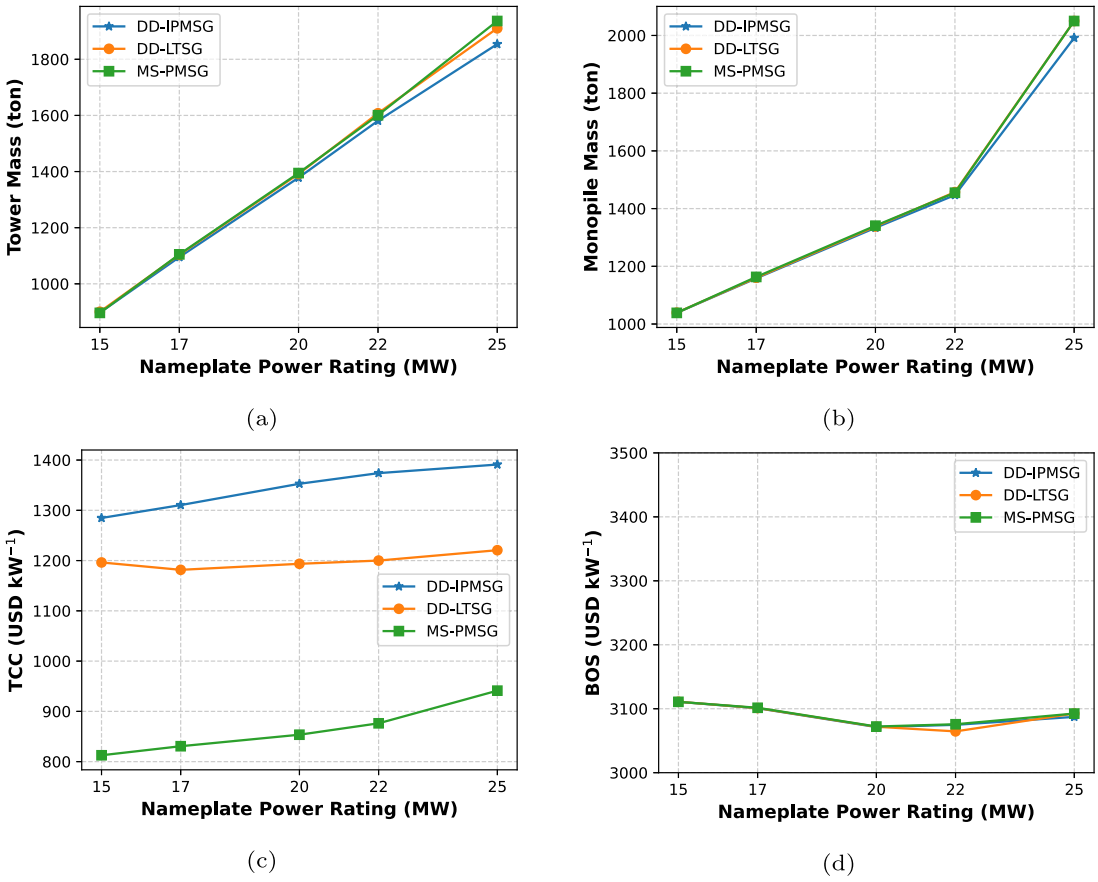

Fig. 8. Solutions for the fixed-bottom designs in terms of mass of the tower and monopile, TCC, and BOS.

both applications and any differences are due to drivetrain-generator technology efficiency. These AEP results are shown in Fig. 7 and demonstrate the value of the higher rated efficiency of the DD-LTSG approach (97%) compared to the DD-IPMSG (95%) or MS-PMSG approach (96% for both the generator and gearbox). It is difficult to discern in Fig. 7, but the green line for the MS-PMSG is slightly below that of the blue line for the DD-IPMSG.

3.4. Wind turbine CapEx, LCOE, and sensitivity analysis

Results for the 15 fixed-bottom designs are reported in Fig. 8 in terms of mass of the tower and monopile, TCC, and BOS. The tower and monopile masses in fixed-bottom designs are only mildly sensitive to variations in the mass of the rotor-nacelle assembly and their design was dominated by the aerodynamic thrust loading coming from the rotor. Therefore, when aggregating all of the wind turbine costs, the distinctions between the designs stem from the differences in the nacelle costs in Fig. 6d. Meaning, generator cost has much greater leverage on the overall TCC (and LCOE) than its mass does via the load path for fixed-bottom applications. This design trend, with its significant LCOE implications, should be verified using higher fidelity loads modeling in future studies. Nevertheless, in this work, with little variation in tower and monopile mass or sizing due to the generator, BOS values do not show noticeable variations across technologies.

The equivalent results for the 15 floating designs are depicted in Fig. 9. Here, there is more spread between the different drivetrain-generator technologies in tower mass and platform mass. Therefore, in contrast to the fixed-bottom application, there is still a benefit to lighter-weight nacelles for floating applications. This observation is also reflected in the TCC trends in Fig. 9c, compared to Fig. 8c. As with the fixed-bottom case, there is little differentiation in BOS costs by drivetrain-generator technology, but the pronounced downward slope in BOS costs with increasing turbine rating is noticeable. This difference is because the floating platform is a significant contributor to the overall BOS cost, more so than monopiles, and higher power ratings means fewer wind turbines for a 600 MW farm and fewer floating platforms.

3.5. LCOE comparison and sensitivity

The final LCOE comparisons for both fixed-bottom and floating applications are found in Fig. 10. We project the LCOE for offshore wind energy to be less than $86/MWh for fixed-bottom designs and $96/MWh for floating designs. An important aspect to observe is that WISDEM predicts fairly flat LCOE trends for fixed-bottom designs across nameplate power ratings, with LCOE rising for all technologies at 25 MW. This trend can be explained by combining the slightly increasing TCC with flat BOS costs and could signal an optimal rating around 20 MW, although such a prediction is beyond the scope of this study and would require greater scrutiny to verify. On the other hand, floating designs show a monotonically declining trend in LCOE, with an exception for the MS-PMSG line. In this case, the higher nameplate power ratings led to a greater reduction in BOS costs that outweighed any increase in TCC.

Across the drivetrain-generator technologies, DD-LTSG has the potential to reduce LCOE by 2%–3% compared to DD-IPMSG, which struggles at power ratings exceeding 17 MW in fixed-bottom settings. For floating offshore wind turbines, DD-LTSG can do even better with 3%–5% reduction in LCOE. However, for both fixed-bottom and floating designs, the MS-PMSG can result in the lowest LCOE, with reductions of up to 7% when compared to DD-IPMSG. Fig. 10b shows the DD-LTSG approaching the MS-PMSG curve by the 25 MW rating; however, it is

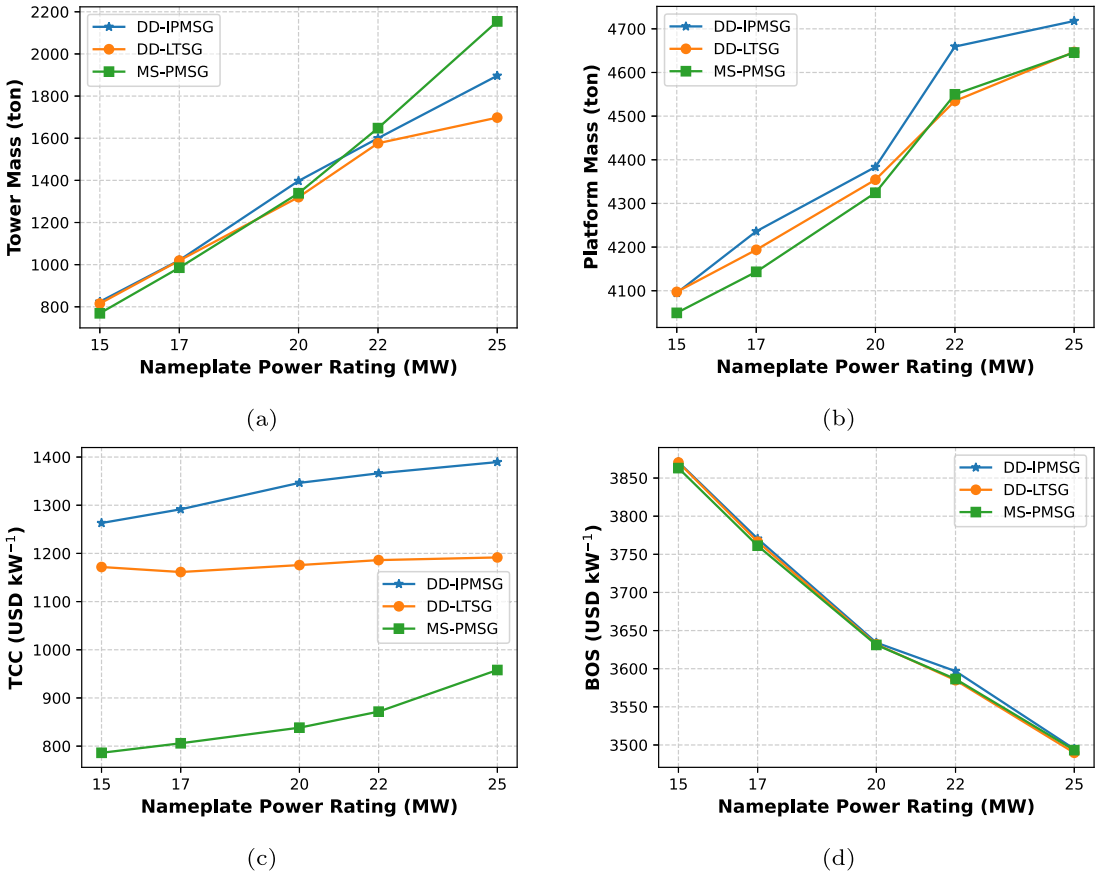

Fig. 9. Solutions for the floating designs in terms of mass of the tower and monopile, TCC, and BOS.

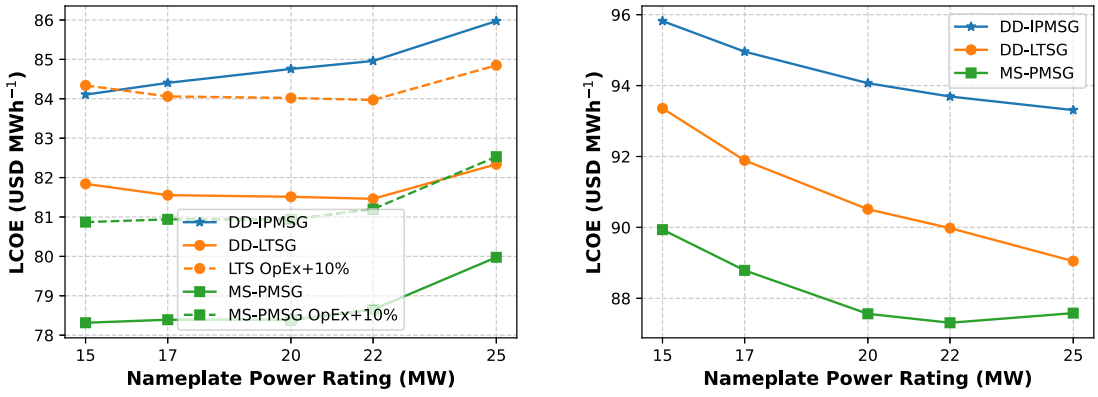

Fig. 10. LCOE comparison between generator technologies for fixed-bottom and floating applications.

likely best to consider the two technologies as roughly equivalent at that point due to our low-fidelity approach to gearbox design.

As mentioned earlier, we made a key assumption that the O&M costs are identical across drivetrain-generator technologies and constant across the different power ratings. However, LCOE can be quite sensitive to O&M costs and it is worth exploring sensitivities to understand the impact of O&M costs on our conclusions. For example, if a 10% increase in O&M costs were necessary for gearbox maintenance, then it takes on the dashed line in Fig. 10a, and the MS-PMSG technology would perform similarly to the DD-LTSG technology as measured by LCOE. If the O&M costs for the DD-LTSG were also to increase due to maintenance needs for the cryogenic system or the armature brushes, then the DD-LTSG system loses the competitive advantage over DD-IPMSG despite its lower weight and capital cost.

The O&M cost sensitivity exploration should be taken as an example of the uncertainties in this work, rather than a summary estimate of error bars on the results. As with any new technology, there are other associated cost uncertainties that are not fully explored here. These uncertainties include differences in manufacturing costs, both factory tooling and labor, and others. Furthermore, the fluctuating prices in commodities, especially for rare-earth magnets with vulnerable supply chains, make even established technology costs a moving target that could shift the results presented here.

4. Conclusions and future work

In this study, we evaluated the prospects of emerging generator technologies for large 15+ MW offshore wind turbines through a conceptual design and optimization to assess the impact on LCOE. The analyses showed a flat LCOE trend versus turbine rating (15–25 MW) for fixed-bottom applications, but a continuously declining trend for floating applications. For current prices of permanent magnets and superconducting wires, DD-LTSGs have the potential to lower LCOE by 2%–3% for fixed-bottom designs and 3%–5% for floating offshore wind turbines relative to DD-IPMSG designs. However, MS-PMSG can result in the lowest LCOE with reductions of up to 7% for both fixed-bottom and floating designs, as long as the gearbox does not increase O&M costs, which we assumed to be constant for all technologies. LTSG solutions have the additional benefit of nearly eliminating rare-earth metals from the generator supply chain, which is a benefit we could not quantify in this analysis. The analysis also showed smaller-than-expected sensitivity to tower-top mass as a driving factor in the LCOE summation. Essentially, at the scale of 15- to 25 MW turbines, the rotor thrust loads are the biggest driver of support structure design, more so than the inertial gravity loads at the tower top. This trend was clearly evident in the fixed-bottom designs, and to a lesser extent, in the floating results as well. However, given the early stage in deployment of all of the technologies for offshore wind turbines at 15+ MW and beyond, real design and operational data from offshore wind farms in the coming years will shed more light on these cost trends. In the meantime, further work is planned on the development and testing of a full-scale DD-LTSG prototype [49].

CRediT authorship contribution statement

Garrett E. Barter: Conceptualization, Formal analysis, Methodology, Software, Writing – original draft, Writing – review & editing. **Latha Sethuraman:** Conceptualization, Methodology, Software, Supervision, Writing – original draft. **Pietro Bortolotti:** Conceptualization, Formal analysis, Methodology, Software, Writing – original draft. **Jonathan Keller:** Funding acquisition, Project administration, Resources, Supervision, Validation, Writing – review & editing. **David A. Torrey:** Conceptualization, Funding acquisition, Methodology, Resources, Supervision, Validation, Writing – review & editing.

Declaration of competing interest

The authors declare that they have no known competing financial interests or personal relationships that could have appeared to influence the work reported in this paper.

Data availability

Data will be made available on request.

Acknowledgments

The authors would like to gratefully acknowledge the support from D. Meeker for technical assistance with FEMM, ALTAIR for 3D modeling of LTS generators, and Bruker for providing data for LTS wire. Also, the support of NREL researchers Mayank Chetan and Daniel Zalkind was instrumental to achieving accurate design optimization of the floating platforms.

This work was authored in part by the National Renewable Energy Laboratory, operated by Alliance for Sustainable Energy, LLC, for the U.S. Department of Energy (DOE) under Contract No. DE-AC36-08GO28308 as part of DE-FOA-0001981. Funding provided by the U.S. Department of Energy, Office of Energy Efficiency and Renewable Energy, Wind Energy Technologies Office, United States. The views expressed in the article do not necessarily represent the views of the DOE or the U.S. Government. The U.S. Government retains and the publisher, by accepting the article for publication, acknowledges that the U.S. Government retains a nonexclusive, paid-up, irrevocable, worldwide license to publish or reproduce the published form of this work, or allow others to do so, for U.S. Government purposes. A portion of the research was performed using computational resources sponsored by the U.S. Department of Energy's Office of Energy Efficiency and Renewable Energy and located at NREL.

References

[1] Musial Walter, Spitsen Paul, Duffy Patrick, Beiter Philipp, Marquis Melinda, Hammond Rob, et al. Offshore wind market report: 2022 edition. Tech. Rep. NREL/TP-5000-83544, Golden, CO: National Renewable Energy Laboratory; 2022, http://dx.doi.org/10.2172/1883382.

[2] Durakovic Adnan. General electric signs rare earths agreement with arafura. 2022, offshoreWIND.biz. URL www.offshorewind.biz/2022/07/13/general-electric-signs-rare-earths-agreement-with-arafura/.

[3] Nejad AR, Keller J, Guo Y, Sheng S, Polinder H, Watson S, et al. Wind turbine drivetrains: State-of-the-art technologies and future development trends. Wind Energy Sci 2022;7(1):387–411. http://dx.doi.org/10.5194/wes-7-387-2022.

[4] Richard Craig. GreenSpur wind designs 15 MW offshore turbine generator without rare earth magnets. Wind Power Mon 2022. URL www.windpowermonthly.com/article/1794342/greenspur-wind-designs-15mw-offshore-turbine-generator-without-rare-earth-magnets.

[5] de Vries Eize. WindTech: ZF modular concept scalable for 15 MW turbine. Wind Power Mon 2018. URL www.windpowermonthly.com/article/1458060/windtech-zf-modular-concept-scalable-15mw-turbine.

[6] Almandoz Gaizka, Gómez Iratxo, Ugalde Gaizka, Poza Javier, Escalada Ana Julia. Study of demagnetization risk in PM machines. IEEE Trans Ind Appl 2019;55(4):3490–500. http://dx.doi.org/10.1109/TIA.2019.2904459.

[7] Chen H, Qu R, Li J. Rotor design of a 7 MW interior permanent magnet wind generator considering demagnetization. In: 2015 IEEE international magnetics conference. 2015, p. 1. http://dx.doi.org/10.1109/INTMAG.2015.7156881.

[8] Chen H, Qu R, Li J, Zhao B. Comparison of interior and surface permanent magnet machines with fractional slot concentrated windings for direct-drive wind generators. In: 2014 17th International conference on electrical machines and systems. Hangzhou, China; 2014, p. 2612–7.

[9] de Vries Eize. Exclusive: How Vestas beat rivals to launch first 15 MW offshore turbine. Wind Power Mon 2021. URL www.windpowermonthly.com/article/1706924/exclusive-vestas-beat-rivals-launch-first-15mw-offshore-turbine.

[10] Turnbull Alan, McKinnon Conor, Carrol James, McDonald Alasdair. On the development of offshore wind turbine technology: An assessment of reliability rates and fault detection methods in a changing market. Energies 2022;15(9). http://dx.doi.org/10.3390/en15093180.

[11] Barter Garrett E, Robertson Amy, Musial Walter. A systems engineering vision for floating offshore wind cost optimization. Renew Energy Focus 2020;34:1–16. http://dx.doi.org/10.1016/j.ref.2020.03.002.

[12] Jung Ga-Eun, Sung Hae-Jin, Dinh Minh-Chau, Park Minwon, Shin Hyunkyoung. A comparative analysis of economics of PMSG and SCSG floating offshore wind farms. Energies 2021;14(5). http://dx.doi.org/10.3390/en14051386.

[13] Zhou C, Yagotintsev KA, Gao P, Haugan TJ, van der Laan DC, Nijhuis A. Critical current of various REBCO tapes under uniaxial strain. IEEE Trans Appl Supercond 2016;26(4):1–4. http://dx.doi.org/10.1109/TASC.2016.2535202.

[14] Abrahamsen Asger Bech, Liu Dong, Magnusson Niklas, Thomas Arwyn, Azar Ziad, Stehouwer Ewoud, et al. Comparison of levelized cost of energy of superconducting direct drive generators for a 10-MW offshore wind turbine. IEEE Trans Appl Supercond 2018;28(4):1–5. http://dx.doi.org/10.1109/TASC.2018.2810294.

[15] Moore Samuel K. Rough seas for the superconducting wind turbine: To keep offshore turbines light, engineers look beyond superconductors to a new permanent-magnet tech. IEEE Spectr 2018;55(8):32–9. http://dx.doi.org/10.1109/MSPEC.2018.8423581.

[16] Song Xiaowei, Bührer Carsten, Mølgaard Anders, Andersen Rasmus S, Brutsaert Patrick, Bauer Markus, et al. Commissioning of the world's first full-scale MW-class superconducting generator on a direct drive wind turbine. IEEE Trans Energy Convers 2020;35(3):1697–704. http://dx.doi.org/10.1109/TEC.2020.2982897.

[17] Dodd Jan. Rethinking the use of rare-earth elements. Wind Power Mon 2018. URL www.windpowermonthly.com/article/1519221/rethinking-use-rare-earth-elements.

[18] Liu Dong. Increasing the feasibility of superconducting generators for 10 MW direct-drive wind turbines [Ph.D. thesis], Delft, The Netherlands: Delft University of Technology; 2017, http://dx.doi.org/10.4233/uuid:074d4f96-e7bf-4dde-a7b4-86c9dd2e214f.

[19] Wang Jin, Qu Ronghai, Tang Yuejin, Liu Yingzhen, Zhang Bin, He Jie, et al. Design of a superconducting synchronous generator with LTS field windings for 12 MW offshore direct-drive wind turbines. IEEE Trans Ind Electron 2016;63(3):1618–28. http://dx.doi.org/10.1109/TIE.2015.2415758.

[20] Cho Han-Wook, Bang Tae-Kyoung, Lee Jeong-In, Shin Kyung-Hun, Lee Hu-Seung, Hur Jin-Seok, et al. Design and preliminary experiments of a rotating armature partial superconducting air-core generator. IEEE Trans Appl Supercond 2022;32(6):1–5. http://dx.doi.org/10.1109/TASC.2022.3180309.

[21] Hoang Trung-Kien, Quéval Loïc, Vido Lionel, Nguyen Dinh-Quang. Levelized cost of energy comparison between permanent magnet and superconducting wind generators for various nominal power. IEEE Trans Appl Supercond 2022;32(7):1–6. http://dx.doi.org/10.1109/TASC.2022.3181996.

[22] Zalkind Daniel, Abbas Nikhar J, Barter Garrett, Bortolotti Pietro, Jasa John, Mudafort Rafael M, et al. Wind energy with integrated servocontrol (WEIS). 2022, http://dx.doi.org/10.5281/zenodo.7150136, GitHub repository. URL http://github.com/WISDEM/WEIS.

[23] Gaertner Evan, Rinker Jennifer, Sethuraman Latha, Zahle Frederik, Anderson Benjamin, Barter Garrett, et al. Definition of the IEA 15-Megawatt offshore reference wind turbine. Tech. Rep. NREL/TP-75698, International Energy Agency; 2020, http://dx.doi.org/10.2172/1603478.

[24] Allen Christopher, Viselli Anthony, Dagher Habib, Goupee Andrew, Gaertner Evan, Abbas Nikhar, et al. Definition of the UMaine VolturnUS-S reference platform developed for the IEA Wind 15-Megawatt offshore reference wind turbine. Tech. Rep. NREL/TP-76773, International Energy Agency; 2020, http://dx.doi.org/10.2172/1660012.

[25] National Renewable Energy Laboratory. WISDEM GeneratorSE. 2022, GitHub repository. URL http://github.com/WISDEM/GeneratorSE.

[26] Meeker David. Finite element method magnetics (FEMM). 2019, URL www.femm.info. v4.2.

[27] Meeker David. pyFEMM - a Python interface to FEMM. 2021, URL www.femm.info/wiki/pyFEMM. v0.1.3.

[28] Carpenter Alberta, Mann Margaret, Gelman Rachel, Lewis John, Benson David, Cresko Joe, et al. Materials flows through industry tool to track supply chain energy demand. In: Proceedings of the LCA XIV international conference. San Francisco, CA; 2014, p. 142.

[29] US Bureau of Labor Statistics. Total factor productivity: Detailed industries in manufacturing, air transportation, and line-haul railroads. 2022, URL www.bls.gov/productivity/tables/.

[30] Gray Justin S, Hwang John T, Martins Joaquim RRA, Moore Kenneth T, Naylor Bret A. OpenMDAO: An open-source framework for multidisciplinary design, analysis, and optimization. Struct Multidiscip Optim 2019;59(4):1075–104. http://dx.doi.org/10.1007/s00158-019-02211-z.

[31] Powell Michael JD. A direct search optimization method that models the objective and constraint functions by linear interpolation. In: Advances in optimization and numerical analysis. Springer; 1994, p. 51–67.

[32] Powell Michael JD. Direct search algorithms for optimization calculations. Acta Numer 1998;7:287–336.

[33] Johnson Steven G. The NLopt nonlinear-optimization package. 2021, URL http://github.com/stevengj/nlopt. v2.7.1.

[34] Sethuraman Latha, Torrey David, Bortolotti Pietro, Barter Garrett. Optimization and comparison of modern offshore wind turbine generators using GeneratorSE 2.0. In: 14th IEEE international electric machines and drives conference. 2023 [in press].

[35] Windings Inc. V-Shape IPM rotors design consideration and concerns. Tech. Rep., 2020, URL www.windings.com/wp-content/uploads/ipm-rotor-considerations-guide.pdf.

[36] Arnold Magnetic Technologies. N48SH data sheet. Tech. Rep., 2022, URL www.arnoldmagnetics.com/wp-content/uploads/2017/11/N48SH-151021.pdf.

[37] Sethuraman Latha, Dykes Katherine L. GeneratorSE: A sizing tool for variable-speed wind turbine generators. Tech. Rep. NREL/TP-5000-66462, Golden, CO: National Renewable Energy Laboratory; 2017, http://dx.doi.org/10.2172/1395455.

[38] Bruker EST. NbTi conductors data sheet. 2021, (Made available via email inquiry).

[39] Ollendorff F. Magnetostatik der massekerne, vol. 25, Arch. Elektrotechnik; 1931, p. 436–47.

[40] Richard Craig. GE eyes offshore wind turbines with superconducting generator. Wind Power Mon 2022. URL www.windpowermonthly.com/article/1749355/ge-eyes-offshore-wind-turbines-superconducting-generator.

[41] Gill Philip E, Murray Walter, Saunders Michael A. SNOPT: An SQP algorithm for large-scale constrained optimization. SIAM Rev 2005;47(1):99–131. http://dx.doi.org/10.1137/S0036144504446096.

[42] Hall Matthew, Housner Stein, Zalkind Daniel, Bortolotti Pietro, Ogden David, Barter Garrett. An open-source frequency-domain model for floating wind turbine design optimization. J Phys Conf Ser 2022;2265(4):042020. http://dx.doi.org/10.1088/1742-6596/2265/4/042020.

[43] Det Norske Veritas. Buckling strength of shells: Recommended practice. Tech. Rep. DNV-RP-C202, 2017, URL dnv.com/oilgas/download/dnv-rp-c202-buckling-strength-of-shells.html.

[44] Stehly Tyler, Duffy Patrick. 2020 cost of wind energy review. Tech. Rep. NREL/TP-5000-81209, Golden, CO: National Renewable Energy Laboratory; 2021, http://dx.doi.org/10.2172/1838135.

[45] Bortolotti Pietro, Berry Derek S, Murray Robynne, Gaertner Evan, Jenne Dale S, Damiani Rick R, et al. A detailed wind turbine blade cost model. Tech. Rep. NREL/TP-5000-73585, Golden, CO: National Renewable Energy Laboratory; 2019, http://dx.doi.org/10.2172/1529217.

[46] Farkas József, Jármai Károly. Optimum design of steel structures. Springer; 2013.

[47] Nunemaker Jacob, Shields Matthew, Hammond Robert, Duffy Patrick. ORBIT: Offshore renewables balance-of-system and installation tool. Tech. Rep. NREL/TP-5000-77081, Golden, CO: National Renewable Energy Laboratory; 2020, http://dx.doi.org/10.2172/1660132.

[48] Siemens Gamesa Renewable Energy. Powered by change: Siemens Gamesa launches 14 MW offshore direct drive turbine with 222-meter rotor. 2020, URL www.siemensgamesa.com/en-int/newsroom/2020/05/200519-siemens-gamesa-turbine-14-222-dd.

[49] Wind Energy Technologies Office. DOE announces additional funding for high-efficiency lightweight generator demonstration. 2021, URL www.energy.gov/eere/wind/articles/doe-announces-additional-funding-high-efficiency-lightweight-generator.